JOURNAL OF GEOPHYSICAL RESEARCH, VOL. 113, D11105, doi:10.1029/2007JD009276, 2008

Atmosphere-ocean conditions jointly guide convection of the Boreal Summer Intraseasonal Oscillation: Satellite observations

Bo Yang,[1] Xiouhua Fu,[1] and Bin Wang[1]

Received 3 August 2007; revised 30 November 2007; accepted 11 March 2008; published 5 June 2008.

[1] The water-vapor and air-temperature profiles from the Atmospheric Infrared Sounder (AIRS), in combination with surface wind from Quick Scatterometer (QuikSCAT) and rainfall and sea surface temperature (SST) from Tropical Rainfall Measurement Mission (TRMM) Microwave Imager (TMI), are used to document surface conditions and vertical moist thermodynamic structures of the 2003–2006 Boreal Summer Intraseasonal Oscillation (BSISO) over the Indo-Pacific warm pool. The composite based on Wheeler and Hendon's intraseasonal oscillation index reveals that Convective Available Potential Energy (CAPE), SST, and surface convergence lead convection in both northward and eastward directions. The preconditioning of CAPE is much earlier than that of SST, implying that the atmosphere internal processes precondition CAPE. On the other hand, the ocean positively feeds back to the atmosphere from bottom up, forming a smooth transition from boundary layer moistening, shallow convection at lower or middle level, to the deep convection all through the troposphere. The preconditioning of the boundary layer moist (dry) anomalies to the subsequent positive (negative) rainfall maximum is as far as 60–90 degrees in longitude (15 degrees in latitude) and quarter-to-half cycle in time. In contrast, this boundary layer preconditioning is virtually undetected from conventional NCEP reanalysis. Finally, the implications of these new findings on the frictional "convective interaction with dynamics" (CID) theory of intraseasonal oscillation are also discussed.

Citation: Yang, B., X. Fu, and B. Wang (2008), Atmosphere-ocean conditions jointly guide convection of the Boreal Summer Intraseasonal Oscillation: Satellite observations, *J. Geophys. Res.*, *113*, D11105, doi:10.1029/2007JD009276.

1. Introduction

[2] The intraseasonal oscillation (ISO) is the strongest regular signal on the subseasonal timescale [*Madden and Julian*, 1971, 1972; *Gualdi et al.*, 1997]. It interacts with adjacent short (weather) and long (climate) timescales and constitutes a pivotal component of the tropical atmospheric variability. In boreal winter, ISO is characterized by the eastward propagating Madden-Julian oscillation [*Madden and Julian*, 1971, 1972] mode. In boreal summer, northward propagating boreal summer intraseasonal oscillation (BSISO) becomes a dominant mode in the Asian–western Pacific summer monsoon system [*Wang and Rui*, 1990a].

[3] The recurrent nature of ISO offers an opportunity to forecast rainfall up to one month in advance [*Waliser et al.*, 2003; *Fu et al.*, 2007]. However, the performance of current ISO dynamical prediction is still well below expectation, primarily owing to the poor understanding and inadequate representation of 3-D moist convection [*Wang and Schlesinger*, 1999; *Fu et al.*, 2006] and atmosphere-ocean interaction [*Flatau et al.*, 1997; *Waliser et al.*, 1999; *Fu et al.*, 2003].

[4] Advancement of ISO studies relies heavily on the improved observations [*Wang et al.*, 2005]. The observed structure of the ISO has been the topic of numerous studies over the past three decades [e.g., *Madden and Julian*, 1971, 1972; *Weickmann*, 1983; *Rui and Wang*, 1990; *Hendon and Liebmann*, 1990; *Hendon and Salby*, 1994; *Lin and Johnson*, 1996; *Jones and Weare*, 1996; *Houze et al.*, 2000; *Yanai et al.*, 2000; *Kemball-Cook and Weare*, 2001; *Kemball-Cook and Wang*, 2001; *Sperber*, 2003; *Kiladis et al.*, 2005]. A number of important properties of the ISO have been identified by using model- dependent reanalysis products (e.g., National Center for Environmental Prediction/National Center for Atmospheric Research (NCEP/NCAR) reanalysis [*Kalnay et al.*, 1996]; European Centre for Medium-Range Weather Forecast (ECMWF) reanalysis [*Gibson et al.*, 1997]), in situ sounding observations (e.g., Tropical Ocean Global Atmosphere Coupled Ocean Atmosphere Response Experiment (TOGA COARE), [*Webster and Lukas*, 1992]; Comprehensive Aerological Reference Data Set (CARDS) [*Eskridge et al.*, 1995]), and satellite observations (e.g., Radiances Measured by the Microwave Sounding Unit (MSU) [*Spencer*, 1993]; Television Infrared observational Satellite (TIROS) Operational Vertical Sounder (TOVS) [*Susskind et al.*, 1997; *Meyers and Waliser*, 2003]) as well as their combinations.

[5] Observational studies to date show that ISO modifies underlying sea surface temperature (SST) primarily through

[1] International Pacific Research Center, University of Hawaii at Manoa, Honolulu, Hawaii, USA.

0148-0227/08/2007JD009276$09.00

changing surface heat fluxes [*Krishnamurti et al.*, 1988; *Lau and Sui*, 1997; *Jones et al.*, 1998; *Wang and Xie*, 1998; *Shinoda et al.*, 1998; *Waliser et al.*, 1999; *Fu et al.*, 2003]. In contrast, the feedback by ocean to the ISO is still not well understood. In the SST warming phase, *Stephens et al.* [2004] hypothesized that the combination of SST warming and enhanced radiative cooling of the upper troposphere favors a destabilization of the atmosphere that is qualified by a sharp increase of Convective Available Potential Energy (CAPE) of the tropical column. Consequently, the ISO is preceded by low-level convergence and development of shallow convection in the lower troposphere, a gradual lofting of moisture into the middle troposphere, and finally a sharp intensification of upward motion and development of deep convection in the upper tropospheric region [*Kiladis et al.*, 2005]. However, these hypotheses have not been proved with concrete observational evidences, mainly owing to the limitations and uncertainties of radiosonde and satellite observations used in previous studies (see *Tian et al.* [2006] for detailed discussion).

[6] The successful launch of satellite Aqua with the Atmospheric Infrared Sounder (AIRS) in late 2002 provided an unprecedented opportunity to monitor the vertical structure of the ISO [*Fu et al.*, 2006; *Tian et al.*, 2006]. With the support of several other satellite data sets (e.g., Quick Scatterometer (QuikSCAT); Advanced Microwave Scanning Radiometer (AMSR_E)), *Fu et al.* [2006] documented the 3-D moisture structures of the 2003–2004 BSISO and its interactions with underlying ocean over the Indo-western Pacific region. The results revealed much larger tropospheric moisture perturbations than those depicted in previous ECMWF analysis and NCEP/NCAR analysis. The positive SST anomaly to the north of active convection, being a response to the stable atmospheric condition in the suppressed phase, can further feedback to the atmosphere through moistening the boundary layer, destabilizing the troposphere, and thus contribute to the northward propagation of the ISO. In an independent study approximately at the same period, *Tian et al.* [2006] used AIRS data (in combination with the precipitation from the Tropical Rainfall Measuring Mission (TRMM)) to characterize the vertical water-vapor and air-temperature structures and spatial-temporal evolution of the ISO in boreal winter. It was shown that the enhanced (suppressed) convection is generally preceded in both time and space by a low-level warm (cold) and moist (dry) anomaly and followed by a low-level cold (warm) and dry (moist) anomaly. Comparison between AIRS and NCEP reanalysis by *Tian et al.* [2006] showed significant differences in the lower troposphere moisture and temperature structure over the Indian and Pacific Oceans, likely due to the limited radiosonde data to constrain the reanalysis and the model-driven errors such as parameterization deficiencies. Overall, the AIRS results obtained by *Tian et al.* [2006] and *Fu et al.* [2006] are consistent with the frictional Kelvin-Rossby wave-conditional instability of the second kind (CISK) model [*Wang*, 1988, 2005; *Wang and Rui*, 1990b; *Wang and Li*, 1994; *Salby et al.*, 1994].

[7] Previous study by *Tian et al.* [2006] focused on the ISO at winter time. Beside the pilot study by *Fu et al.* [2006], a comprehensive investigation on the structure evolution of the BSISO with current available satellite data has not been reported. The objective of current research is to document the spatial and temporal evolution of composite BSISO as well as its coupling with underlying ocean through synergistic use of various satellite observations in the atmosphere and at the ocean surface (Aqua/AIRS air temperature and water vapor; TRMM TMI SST and rainfall; QuikSCAT surface wind). Particular attention will be given to the phase relationship between vertical moist thermodynamic field, CAPE, SST, large-scale convergence/divergence, and surface rainfall. We hope to combine these current available high-resolution satellite data to improve our understanding of the BSISO, although a complete and coherent picture might not be readily available owing to the limited data period, satellite retrieval uncertainties, and more importantly, the insufficiency in the theoretical understanding this topic. Finally, the result will also be compared with that from conventional global reanalysis.

[8] The outline of this paper is as follow: the data and methodology are introduced in section 2. Section 3 presents the main results. Section 4 summarizes the major findings and the implications of these results to the BSISO theory.

2. Data and Methodology

2.1. Data Sets

[9] The AIRS level 3 version-4 data are used in this study. It is based on retrievals from AIRS and AMSU instruments and provides 3-D structures of the global water vapor and atmosphere temperature with very high spatial and temporal resolution (more description of AIRS instrument, products, and validation is given by *Tian et al.* [2006]). Original AIRS level 3 data have twice daily observations (ascending and descending paths) with a horizontal resolution of one degree by one degree. The vertical grid is based on the World Meteorological Organization (WMO) standard pressure levels from 1000 to 1 hPa for temperature and layers from 1000 to 100 hPa for water vapor [*Tian et al.*, 2006]. In this study, we will use the data from four recent years (2003–2006).

[10] To capture the joint atmosphere-ocean effect on guiding the ISO convection, several other satellite data sets are also used. They include surface wind from Quick Scatterometer (QuikSCAT) version-2, sea surface temperature (SST) and rainfall from Tropical Rainfall Measurement Mission (TRMM) Microwave Imager (TMI) version-4. The data vary in spatial and temporal resolutions. To facilitate the analysis, they are all interpolated to daily data with the horizontal resolution of one degree by one degree.

[11] The ISO index developed by *Wheeler and Hendon* [2004] will be used to determine the phase before making a composite (see also section 2.2). The combinations of fields chosen for calculating the ISO indices are daily averaged outgoing longwave radiation (OLR) from the National Oceanic and Atmospheric Administration (NOAA) polar-orbiting series of satellites, 850 hPa zonal wind (u850) and 200 hPa zonal wind (u200) from NCEP reanalysis, each averaged over the latitudes of 15°S–15°N. Data from 1982 to 2006 are used to define the ISO indices continuously, while only the ISO indices between 2003 and 2006 are extracted for the purpose of phase selection in this composite study.

[12] To compare the composite BSISO vertical structure based on high-resolution satellite data with that from reanalysis products, the daily averaged air-temperature and water-vapor profiles from NCEP reanalysis between 2003 and 2006 are also used. They are analyzed on a 2.5° latitude-longitude grid. The vertical grid is based on the WMO standard pressure levels from 1000 to 100 hPa for temperature and from 1000 to 300 hPa for water vapor. Note that the water vapor from NCEP is reported on the levels while that from AIRS is reported on layers. However, the impacts of this disparity should be small and will not affect the main results of this study.

2.2. Methodology

2.2.1. CAPE Calculation

[13] CAPE is an instability descriptor that represents how powerful the convection might be if it does materialize. Conceptually, CAPE is expressed as the amount of buoyant energy available to speed up a parcel vertically, or the amount of work a parcel does on the environment after it is lifted to the level of free convection. It is calculated by integrating vertically the local buoyancy of a parcel from the level of free convection (LFC) to the equilibrium level (EL). The formal definition is given by

$$CAPE = \int_{Z_f}^{Z_n} g\left(\frac{T_{parcel} - T_{env}}{T_{env}}\right) dz, \qquad (1)$$

where Z_f and Z_n are, respectively, the heights of the levels of free convection and equilibrium (neutral buoyancy), T_{parcel} and T_{env} are the temperatures, respectively, of the specific parcel and the ambient environment, and g is the acceleration due to gravity.

[14] The atmosphere-temperature and water-vapor profiles from the AIRS data set are used to calculate the CAPE. The computed CAPE value can vary significantly depending on the choice of the parcel used. In this study, the specific parcel used for CAPE calculation originates from the 1000hPa level with temperature and specific humidity equal to that of ambient environment.

2.2.2. Composite Procedure

[15] Empirical Orthogonal Function (EOF) analysis is a useful tool for identifying the coherent patterns that can explain the major portion of the total variance of observed field. A single outstanding eigenmode normally represents a standing oscillation; whereas propagation can be described by a pair of outstanding modes whose temporal coefficients [principal components (PCs)] are in quadrature [*Zhang and Hendon*, 1997]. *Wheeler and Hendon* [2004] developed a seasonally independent ISO index based on a leading EOF pair of the combined analysis of near-equatorially averaged 850-hPa zonal wind, 200-hPa zonal wind, and satellite-observed OLR. With the annual cycle and interannual variability being removed in advance, this EOF projection can effectively extract the signal at the intraseasonal timescale. In the present study, the phase separation in the composite process is objectively determined with the Wheeler and Hendon ISO Index.

[16] A pivotal step in this composite study is the necessary prior removal of certain longer-timescale variability and synoptic-scale variability. The influence of longer-timescale components is removed from the NOAA OLR, NCEP reanalysis and high- resolution satellite data by the following two steps. First of all, we subtracted from each grid point the annual mean and first three harmonics of the annual cycle. Second, a 121-day running mean is subtracted to remove variability with timescales longer than intraseasonal. Removal of synoptic-scale variability is done by performing an additional 5-day running mean. Without specific denotation, hereafter all the anomaly fields (e.g., wind, temperature, water vapor, CAPE) are referred to the data after the removal of longer-timescale and synoptic-scale variability.

[17] A detailed description of the EOF analysis and related technical issues is given by *Wheeler and Hendon* [2004]. Although the data period used in their study is from 1979 to 2001, which has several years difference from the period used here, the spatial structure and the power spectra of the leading EOF pair are virtually identical in both studies (figure not shown), indicating the objectiveness and robustness of this EOF method in capturing the coherent structure of ISO.

[18] Time series of PC1 and PC2 for 2003, 2004, 2005 and 2006 are shown in Figure 1. Both PC1 and PC2 are normalized by their 1982–2006 standard deviations. Intraseasonal variations can be clearly identified from these four time series, with PC2 lagging PC1 by 10–15 day [c.f., *Wheeler and Hendon*, 2004, Figure 5]. The conventional definition for boreal summer is from May to October. However, there are several strong cases (1, 4, 8) with the crest right at the beginning of the May. Given the limited number of BSISO events between 2003 and 2006, we extend to April in this study to keep the integrity of these three strong cases and increase the sample size.

[19] Given the quasi-orthogonal nature of the leading PC pair, it is convenient to diagnose the state of the BSISO as a point in the 2-D phase space defined by PC1 and PC2. As an example, Figure 2 shows the (PC1, PC2) phase space points for all available days in the 2004 boreal summer. Points representing sequential days are joined by a line, which traces anticlockwise around the origin most of the time, signifying the eastward propagation of the ISO signal. Following *Wheeler and Hendon* [2004], points falling outside the inner circle (with the amplitude of (PC1, PC2) vectors greater than 1.0) represent the strong ISO days; whereas those falling within the inner circle (with the amplitude of (PC1, PC2) vectors smaller than 1.0) indicate weak ISO days. On the basis of this criterion, a total of 15 major BSISO events are identified from 2003 to 2006 (Figure 1).

[20] The spatial patterns of typical BSISO can be depicted through the use of the composite, which follows the same procedure taken by *Wheeler and Hendon* [2004]. Namely, we composite by taking the average of the observed anomaly fields for the "strong ISO" days that fall within each of the numbered phases of Figure 2 (excluding those "weak ISO" days falling in the inner circle).

3. Results

3.1. Surface Analysis

[21] The composite BSISO cycle reveals coherent spatial-temporal evolution of intraseasonal SST, surface wind and

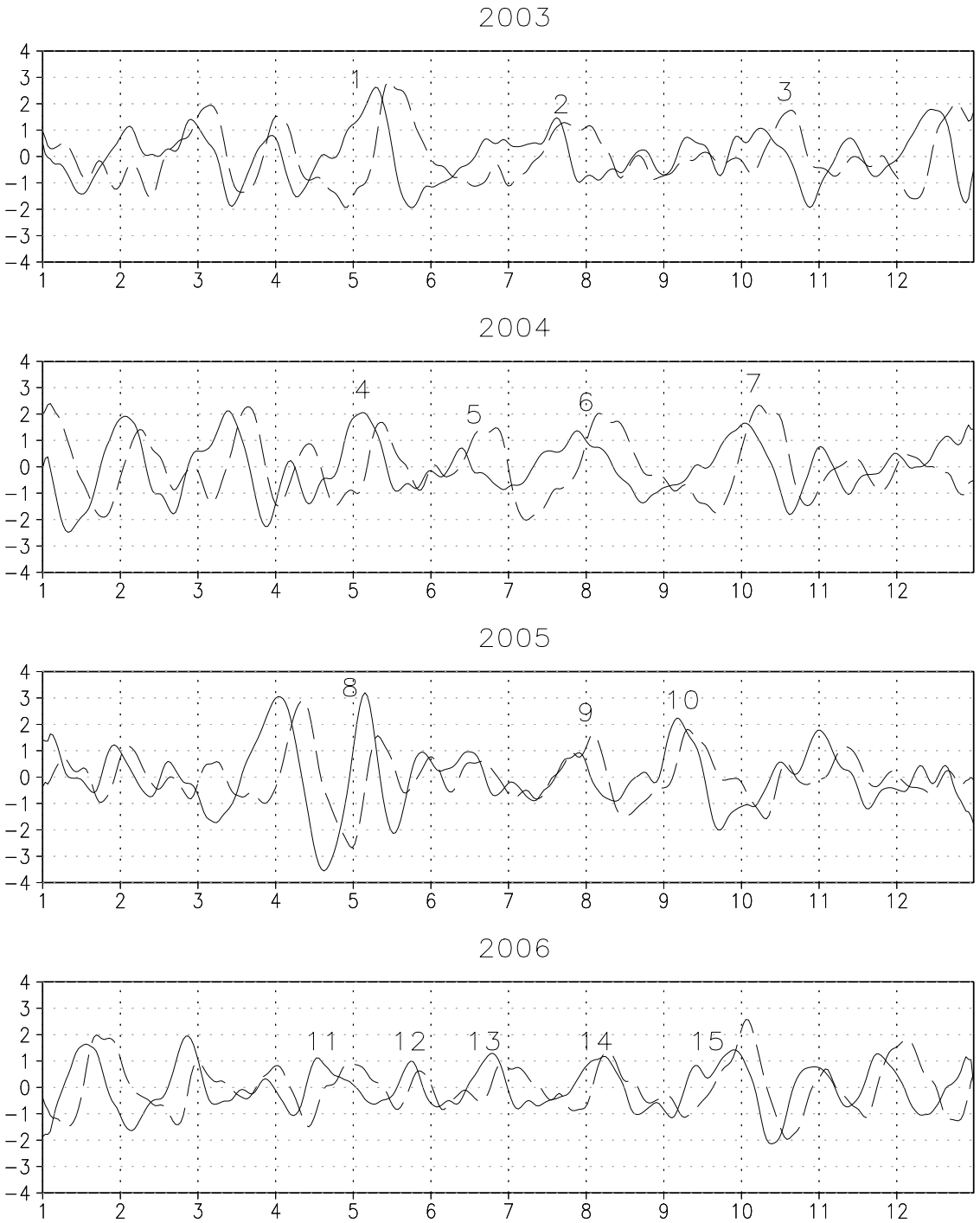

Figure 1. The (normalized) PC1 (solid line) and PC2 (dashed line) time series for the years 2003, 2004, 2005, and 2006. Also labeled (as numbers) is the ordinal number of individual event.

rainfall anomalies in the Indo-Pacific warm pool (Figures 3 and 4). In phase one, a large area including the equatorial western Pacific, Maritime Continent, Bay of Bengal, and part of the equatorial Indian Ocean is dominated by negative rainfall anomalies (suppressed convection). The dry spell produces positive SST anomalies in this suppressed convection area gradually through increasing downward solar radiation and decreasing latent heat flux [*Sengupta and Ravichandran*, 2001; *Fu et al.*, 2003]. Meanwhile, positive rainfall anomalies are observed in the Western North Pacific (WNP), with the rainbands tilting northwest-southeastward. The weak convection of a developing BSISO episode is evident over Africa and the western and central Indian Ocean. Overall, the composite anomalies reveal much greater amplitude than those obtained by *Tian et al.* [2006] and *Fu et al.* [2006], which can be ascribed to the difference in data preprocessing. The anomalies in this study include all the variability from 5 days to 120 days;

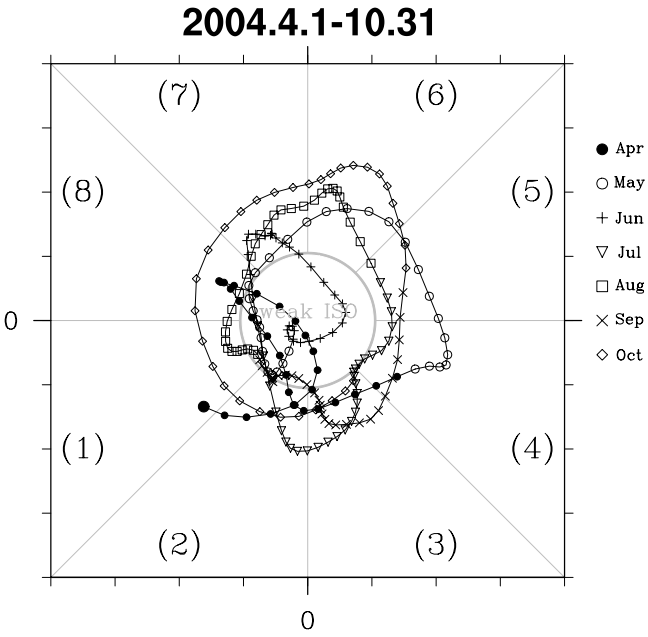

Figure 2. (PC1, PC2) phase space points for all days from April 2004 to October 2004. Eight defined regions of the phase space are labeled, as is the region considered to signify weak ISO activity. Different months are separated with different mark.

whereas those obtained by *Fu et al.* [2006] and *Tian et al.* [2006] are either regressed data or the data filtered to a much narrower frequency domain.

[22] In the subsequent two phases, the Indian Ocean convection gradually builds up and expands eastward. Correspondingly, the original suppressed convection area contracts and moves northeastward to the WNP. The northwest-southeast tilting rainbands in the WNP fade away quickly.

[23] By phase four, the Indian Ocean convection reaches its maximum and starts to bifurcate at the west boundary of the Maritime Continent. In contrast with previous three phases, the SST is now nearly in quadrature with rainfall, with positive SST anomalies leading the convection and negative SST anomalies lagging behind by approximately a quarter of the cycle, implying the time lag between the buildup of the convection and its feedback to the underlying ocean SST. The positive SST anomalies at the leading edge of the northern hemisphere (NH) convection occupy almost the whole Bay of Bengal; whereas their counterparts in the southern hemisphere (SH) are rather weak (Figure 3). The surface circulation associated with the Indian Ocean convection maximum is characterized by typical Gill pattern, with two anomalous cyclonic Rossby gyres lying to the west and anomalous easterly winds extending eastward far away from the convection center. Consistent with the SST asymmetry, the Rossby gyre in the northern hemisphere is considerably stronger and broader than its southern counterpart (Figure 4).

[24] Once the positive rainfall maximum hits the Maritime Continent, it moves off the equatorial region into both hemispheres. The north branch is much stronger than that of the south branch (phase 5), partly owing to larger SST anomalies in the NH than in the SH [*Fu et al.*, 2006]. Meanwhile, the convective anomalies in the Maritime Continent and equatorial western Pacific intensify and extend eastward, linking with the north branch of the Indian Ocean convection and forming a broad northwest-southeast tilting rainband that extends from 80°E to 160°E. This tilting rainband moves northeastward gradually. In phase six, the north branch of the Indian Ocean convection dominates the Bay of Bengal, leaving the entire equatorial Indian Ocean controlled by the suppressed convection. By phase seven, the suppressed convection in the Indian Ocean expands northward and eastward, cutting off the northwest-southeast tilting rainband. Except for a small area at the northeast tip of the Bay of Bengal, the main convection center is shifted to the WNP. Enhanced convection in phase seven is wholly within the anomalous westerlies over the WNP; whereas anomalous easterlies prevail in the suppressed convection area of the equatorial Indian Ocean (Figure 4). Once again, the positive SST anomalies in the Indian Ocean gradually form owing to the increased downward solar radiation and decreased surface evaporation. By phase eight, the WNP convection starts to dissipate, while new convective anomalies emerge off the coast of the Eastern Africa, signifying the end of the current event and presaging the onset of the next one.

3.2. CAPE

[25] Figure 5 shows the composite spatial-temporal evolutions of CAPE and rainfall anomalies. Both the CAPE and rainfall are smoothed spatially to dampen small-scale variability. At the growing phases of the Indian Ocean BSISO (phases 1–2), the broad suppressed convection area including part of the eastern Indian Ocean, Bay of Bengal, Maritime Continent and the equatorial western Pacific is dominated by positive CAPE anomalies; whereas weak negative CAPE anomalies are nearly collocated with the positive rainfall anomalies in the equatorial Indian Ocean. Meanwhile, the surface convergence slightly leads the developing Indian Ocean convection in both east and north directions, with broad region of weak divergence further ahead (Figure 6). The broad area of large-scale subsidence tends to inhibit the development of convection in spite of the presence of large positive CAPE anomalies.

[26] In the mature phase of Indian Ocean convection (phase 4), sustained precipitation consumes up the CAPE through vertical recycling of water vapor, leaving negative CAPE anomalies behind. The observed negative CAPE anomalies are nearly collocated with underlying negative SST anomalies and drying atmosphere boundary layer, which possibly can be ascribed to the precipitating downdrafts under the ISO convection [*Fu et al.*, 2006]. The downdrafts-induced divergence underlying the deep convection can be identified in a nonsmoothed plot (figure not shown). However, they are significantly weaker and narrower when compared to the surrounding convergence and thus can hardly be identified in the spatially smoothed Figure 6. Consequently, surface convergence is nearly collocated with the positive rainfall anomalies, with a slight lead at the east and northeast direction.

[27] In the subsequent three phases (phases 5–7), the enhanced convection gradually shifts to the WNP. The CAPE is almost out of phase with the convection in these three phases. The negative CAPE anomalies nearly coincide

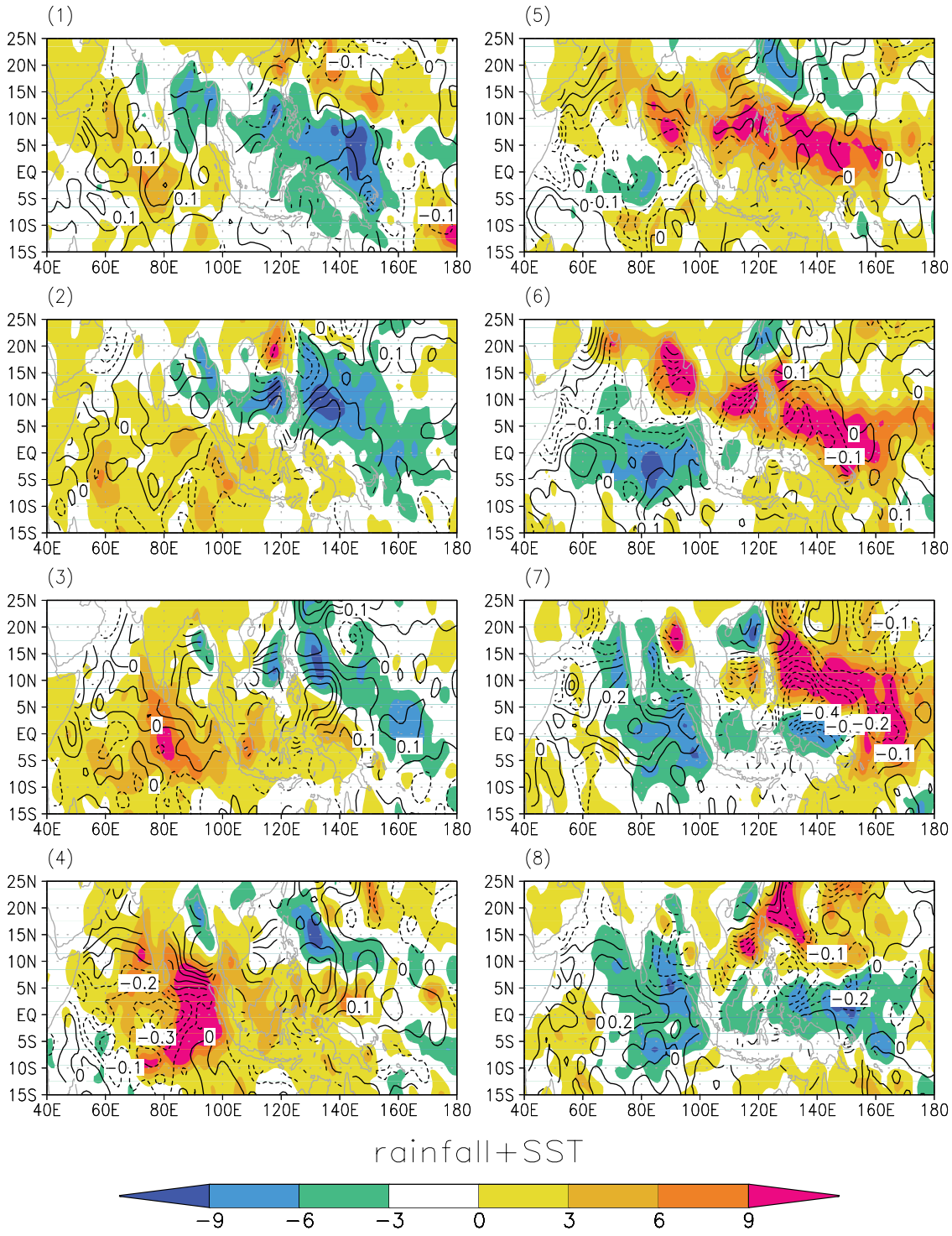

Figure 3. Composite space-time evolutions of rainfall (shaded, mm/d) and SST (contour interval 0.1 K) anomalies (phases (1) to (8)). The rainfall and SST are from TRMM TMI data set.

with positive precipitation anomalies; whereas the positive CAPE anomalies reappear in the Indian Ocean suppressed convection region and gradually extend eastward. Meanwhile, significant convergence also reappears in the western half of Indian Ocean at phases 7 and 8, presaging the beginning of a new ISO episode [e.g., *Wang et al.*, 2005].

[28] The composite results suggest that atmosphere and ocean conditions jointly guide the convection of BSISO, with SST and surface convergence lead rainfall in both zonal and meridional direction (see also underlying polygraphs in Figures 7 and 8). However, the preconditioning of the CAPE is much earlier than that of the SST, suggesting that the atmosphere alone might be able to generate intrinsic mode of ISO.

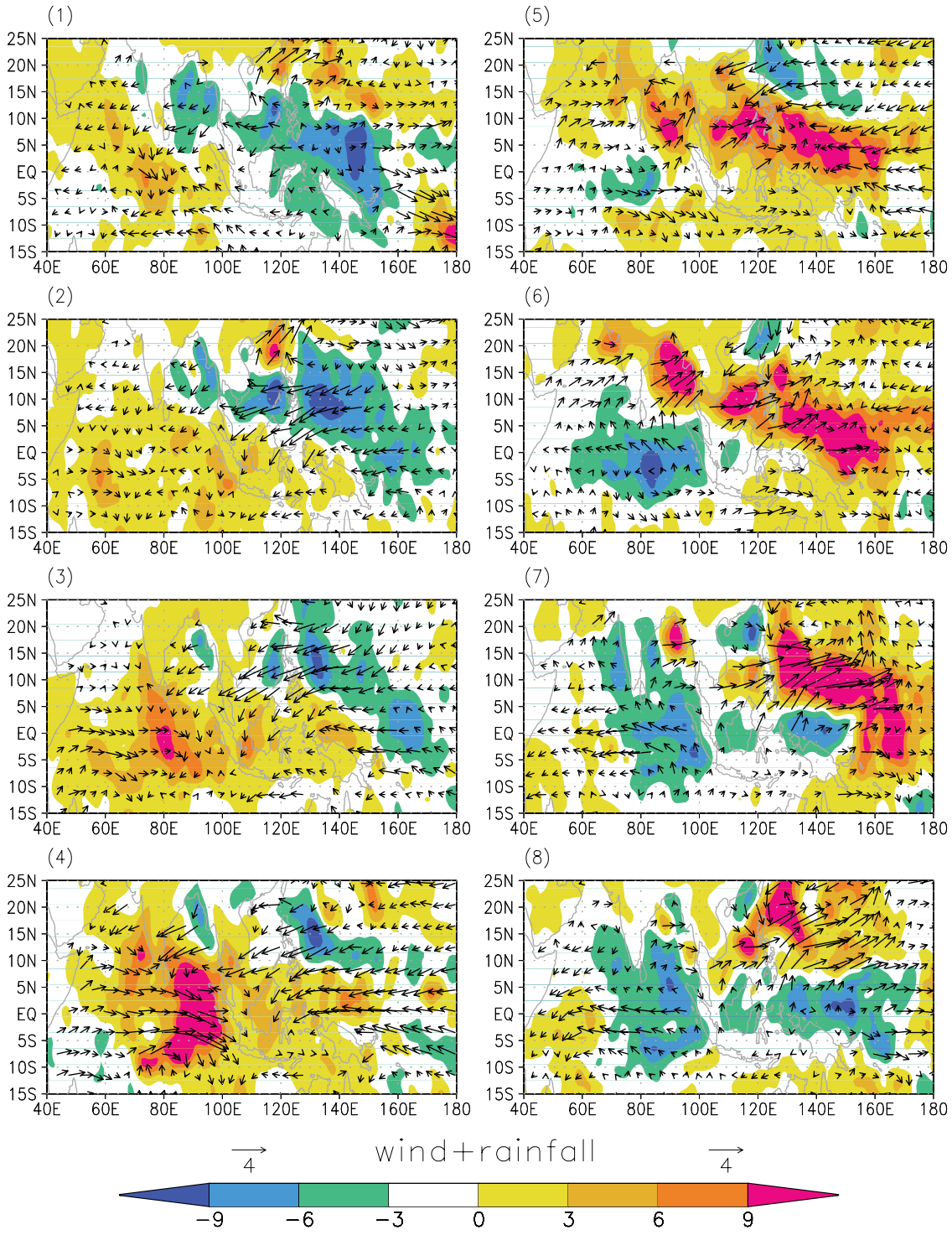

Figure 4. Composite space-time evolutions of rainfall (shaded, mm/d) and surface wind (m/s) anomalies (phases (1) to (8)). The rainfall is from TRMM TMI data set, and surface wind is from QuikSCAT.

3.3. Vertical Structures of the Atmosphere Moist Thermodynamic Field

3.3.1. Pressure-Longitude Cross Section

[29] The moisture field shows markedly different vertical structure as a function of the convection anomaly strength. Similar to the finding for boreal winter by *Tian et al.* [2006], in the region of strongly enhanced (suppressed) convection, moist (dry) anomalies are generally found throughout the atmosphere column except for a very thin layer of dry (moist) anomalies near the surface. *Fu et al.* [2006] conjectured that the drying surface layer underlying strongly enhanced convection could possibly be ascribed to the associated downdrafts. Although retrieval errors can cause

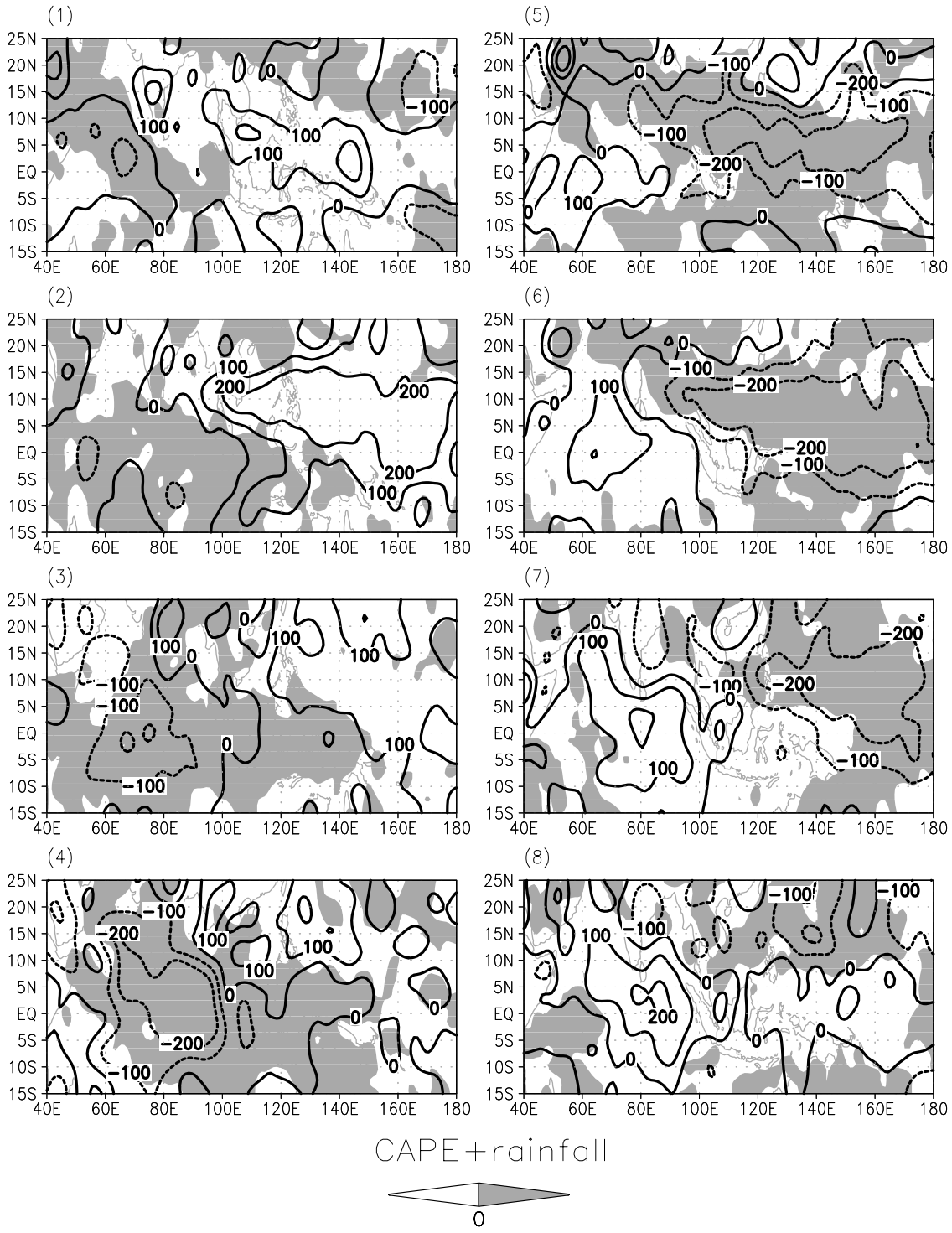

Figure 5. Composite space-time evolutions of CAPE (J/kg, contour) and rainfall (positive area shaded) anomalies (phases (1)–(8)). Both rainfall and CAPE are spatially smoothed to dampen small-scale variability. The contour intervals for CAPE are −200, −100, 0, 100, and 200 J/kg.

the observational uncertainties at the near surface layer, several other independent observational studies also found similar near-surface dry layer under enhanced deep convection, suggesting that it might be real phenomenon instead of retrieval errors [*McBride and Frank*, 1999; *Kemball-Cook and Weare*, 2001; *Mapes et al.*, 2006]. In contrast, there exists a bimodal structure in the weakly enhanced (suppressed) convection region, with moist (dry) anomalies overlying dry (moist) anomalies to the west of positive (negative) precipitation maximum.

[30] Strong enhanced (suppressed) convection is generally preceded by low-level moist (dry) anomalies, and followed by low-level dry (moist) anomalies underneath and to the west. Overall, there is a clear trend of westward tilting of

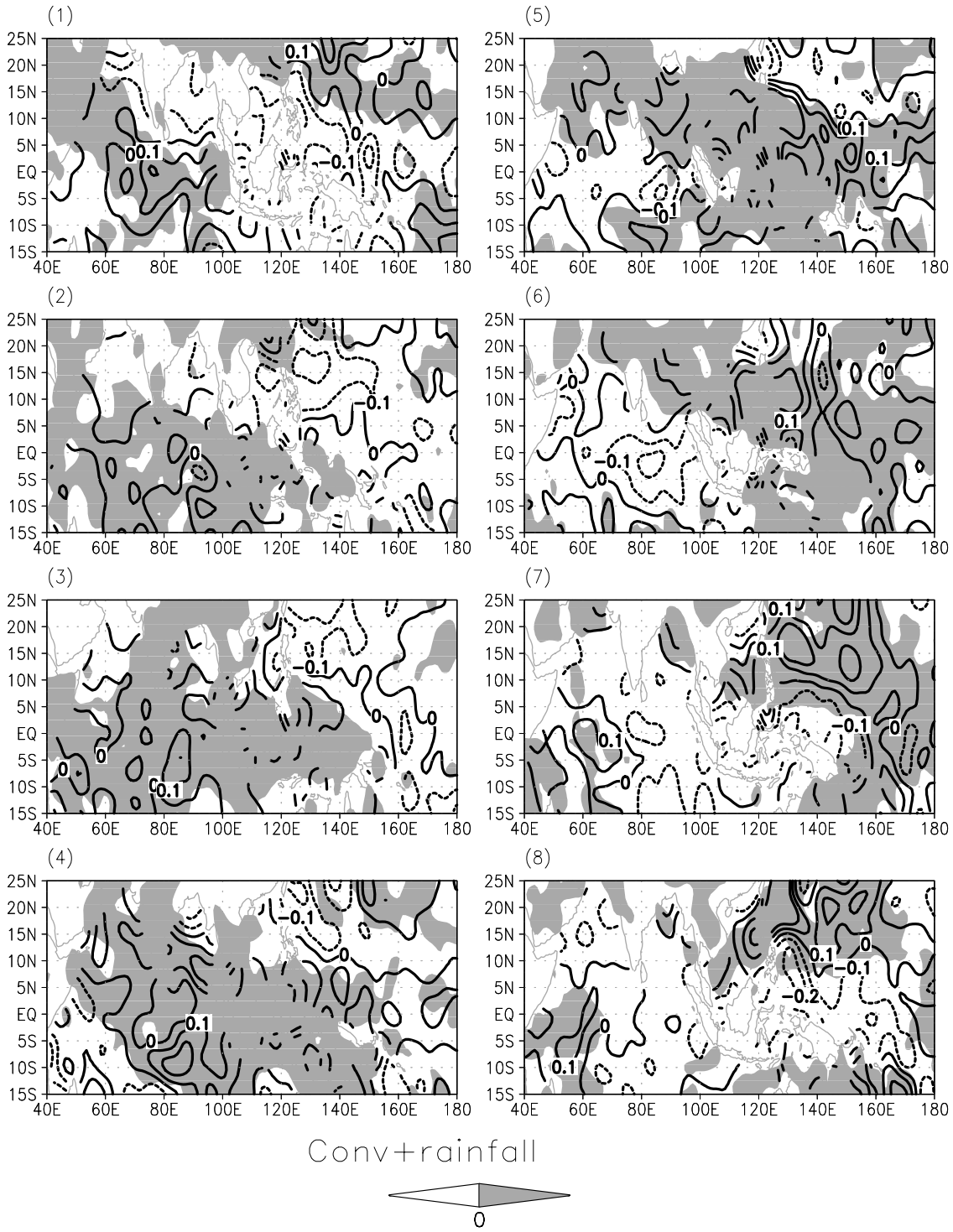

Figure 6. Composite space-time evolutions of surface convergence (10^{-5} s^{-1}, contour) and rainfall (positive areas shaded) anomalies (phases (1)–(8)). Both rainfall and surface convergence are spatially smoothed to dampen small-scale variability. The contour intervals for surface convergence are -0.2×10^{-5}, -0.1×10^{-5}, 0, 0.1×10^{-5}, and 0.2×10^{-5} s^{-1}. Surface convergence is calculated from the QuikSCAT surface wind, which is available over ocean only.

the moisture anomalies, forming a smooth transition from boundary layer moistening, shallow convection at lower or middle level, to the deep convection all through the troposphere. The preconditioning of the moist (dry) anomalies at the boundary layer to the subsequent positive (negative) rainfall maximum is about 60–90 degrees in longitude and quarter-to-half cycle in time, providing the opportunity to forecast rainfall up to one month in advance.

[31] Similar to the moisture preconditioning, the strong enhanced (suppressed) convection is generally preceded by

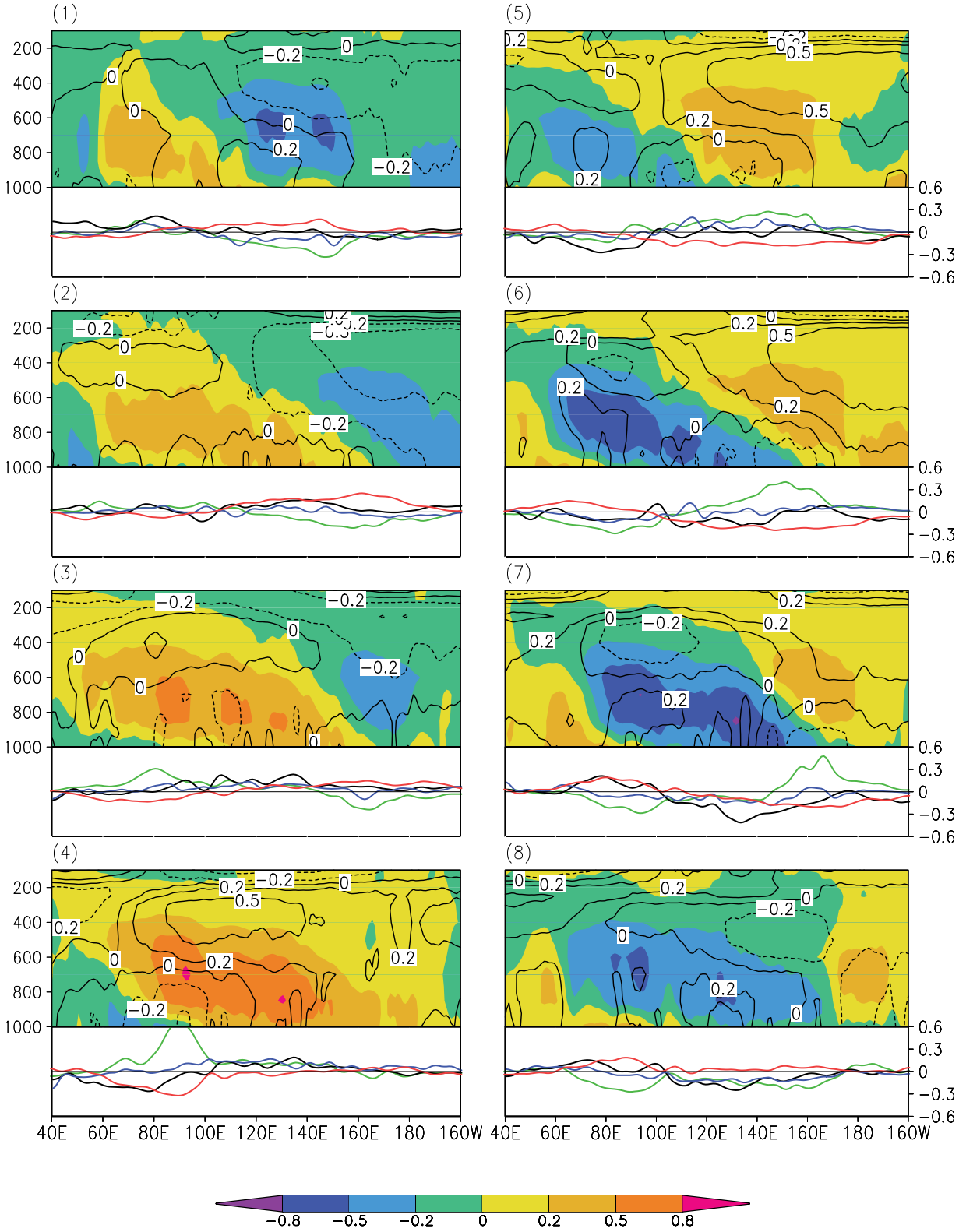

Figure 7. Pressure-longitude cross sections of temperature anomaly (K, contour) and specific humidity anomaly (g/kg, shaded) overlying the associated anomalies (bottom polygraphs) of rainfall (mm/hr, green line), CAPE (10^3 J/kg, red line), SST (K, black line), and surface convergence (10^{-5} s^{-1}, blue line) for the composite BSISO based on AIRS data from 2003 to 2006. The contour (shading) intervals for temperature (specific humidity) anomalies are −0.8, −0.5, −0.2, 0, 0.2, 0.5, and 0.8 K (g/kg), respectively. The anomalies are averaged from 8°S–8°N.

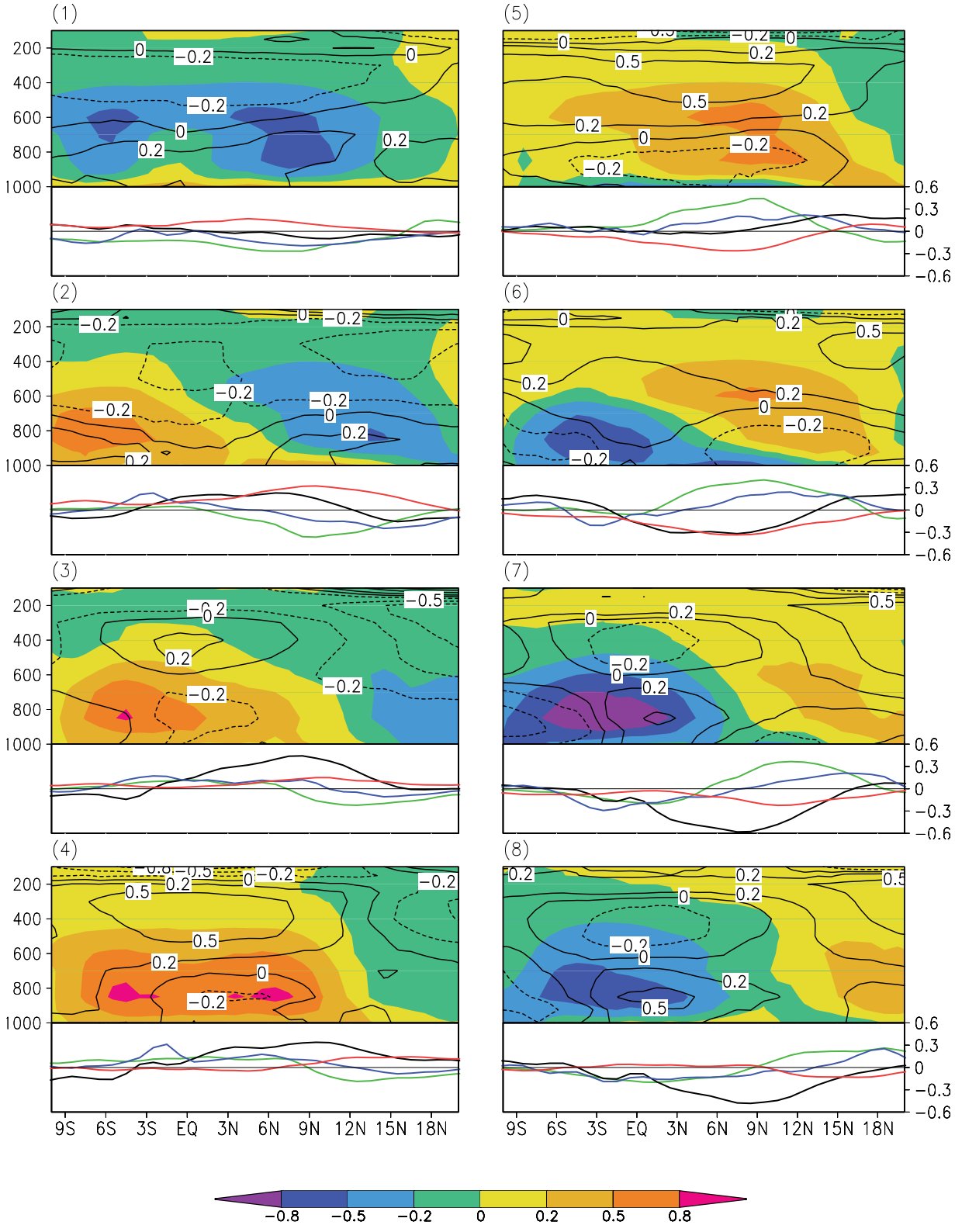

Figure 8. As in Figure 7 but for the pressure-latitude cross sections. The anomalies are averaged from 110°E to 140°E.

a lower tropospheric warm (cold) anomaly and followed by a lower tropospheric cold (warm) anomaly in both time and space. However, there are still certain differences between the temperature and humidity structures in detail. Over the strongly enhanced (suppressed) convection region, the moist (dry) anomalies usually occupy the whole troposphere, with dry (moist) anomalies lying in a very thin layer close to the surface; whereas the transition from warm

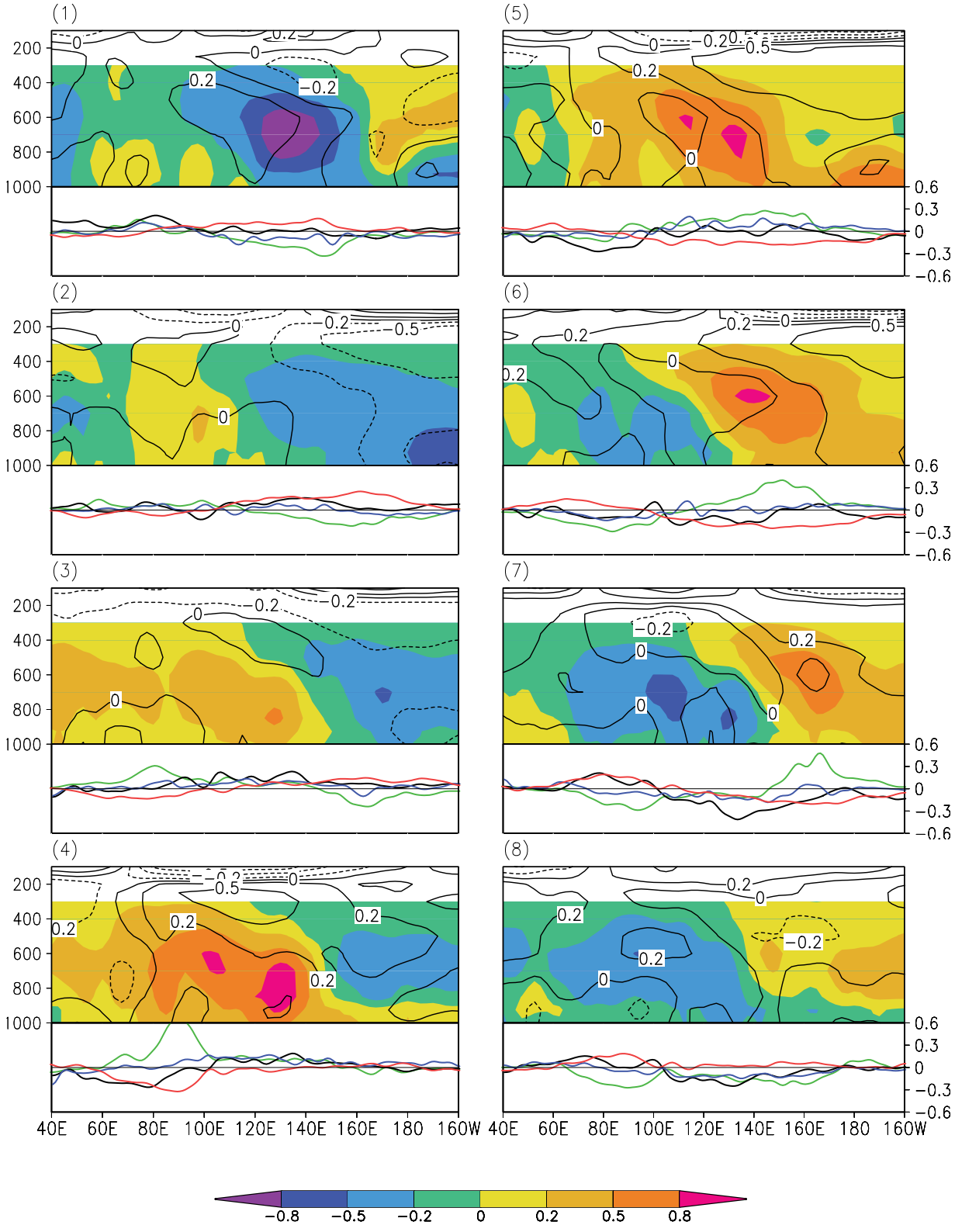

Figure 9. As in Figure 7 but from NCEP data.

(cold) anomalies to cold (warm) anomalies occurs at a much higher altitude around 500–700 hPa. Previous studies by *Tian et al.* [2006] on the wintertime ISO shows a similar vertical structure, although the transition between warm (cold) and cold (warm) anomalies in the troposphere occurs at a relative lower level near 800 hPa.

3.3.2. Pressure-Latitude Cross Section

[32] Figure 8 shows the composite pressure-latitude cross section of moisture and temperature anomalies along with

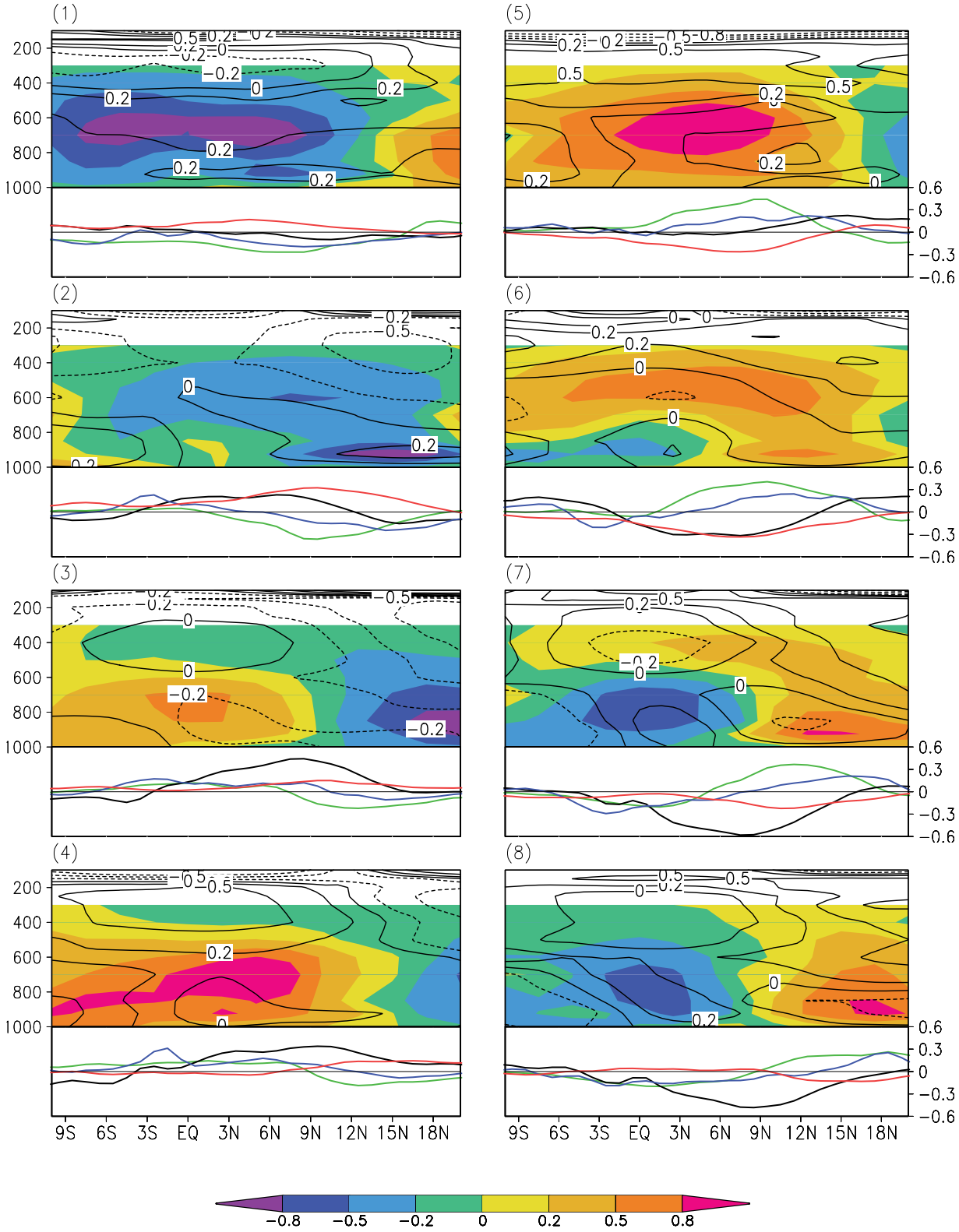

Figure 10. As in Figure 8 but from NCEP data.

CAPE, SST, surface convergence, and rainfall anomalies, averaged between 110°E and 140°E. In phase one, the suppressed convection dominates the equatorial western Pacific with one anomalous dry cell sitting on either side. Over the suppressed convection region between 9°S and 14°N, a trimodal pattern can be identified from the temperature field, with a cold anomaly located between two warm anomalies. The vertical extent of the cold anomaly is confined only to the middle-upper troposphere (600–250 hPa); whereas the dry anomaly occupies almost the

whole atmosphere column. Overall, the CAPE is almost out of phase with the rainfall, with positive CAPE anomalies collocated with negative rainfall anomalies.

[33] In phase two, the south cell of dry anomalies disappears and the north one weakens and moves northward. The preconditioning of moist anomalies is evident under and to the south of suppressed convection. The positive moist anomalies tilt both southward and upward, extending from the surface layer at 15°N to 400 hPa at 3°S. Given the shallowness of the convection at this stage, the precipitation anomalies is still near zero at the equatorial western Pacific. Cold (dry) anomalies overlie warm (moist) anomalies at most of the region, resulting in positive CAPE anomalies between 10°S and 20°N. Overall, CAPE leads SST, surface convergence, and rainfall by about 8, 14, 20 degrees respectively.

[34] By phase three, positive rainfall anomalies are observed between 6°S and 6°N. Meanwhile, positive temperature anomalies appear between 600 hPa and 300 hPa at the same region, signifying the materialization of convection at the upper troposphere. As the convection strengthens and moves northward (phase 4), the lead-lag relationship among CAPE, SST, surface convergence and rainfall still hold although the actual spatial differences (degrees in latitude) among them are decreased. By phase five, collocated with enhanced convection (positive rainfall anomaly) between the equator and 14°N, the positive temperature anomalies overlie negative temperature anomalies with the sharp transition at around 750 hPa. A thin layer of drying anomalies appears underneath the deep convection. The drying anomalies build up and tilt upward and southward (phase 6), preconditioning the suppressed convection at the equatorial western Pacific (phase 7 and 8). By phase eight, the suppressed convection near the equator reaches its mature stage and the southward tilting angle decreased. A clear trimodal temperature anomaly pattern appears with cold anomalies located in the upper troposphere.

[35] Similar to the pressure-longitude cross section, there is a coherent lead-lag relationship among CAPE, SST, surface convergence, and rainfall anomalies. The preconditioning of the moist (dry) anomalies at the surface layer to the subsequent positive (negative) rainfall maximum is as far as 15 degrees in latitude and a quarter-to-half cycle in time. As the enhanced (suppressed) convection moves northward, the southward tilting angle of moist (dry) anomalies is decreased and the preconditioning of moist (dry) anomalies becomes less significant. Meanwhile, the amplitude of maximum positive precipitation anomalies increases, reaching its climax around 10°N. After passing 10°N, the amplitude starts to decrease as the BSISO moves further northward.

3.3.3. Comparison Between AIRS and NCEP

[36] A diagram similar to Figure 7 but based on NCEP is shown in Figure 9. To facilitate comparison, the line plots underlying these pressure-longitude cross sections are the same as that in Figure 7. Below 300hPa, the vertical moisture structures are roughly similar between AIRS and NCEP. The westward tilt of the moist (dry) anomalies with height and their eastward propagation are also captured in NCEP data. However, considerable differences are found over the western Indian Ocean in phases one and two, where the positive moist anomalies from NCEP data are weaker and less organized than their counterparts from AIRS data.

[37] A salient feature of AIRS-observed temperature field, low-level preconditioning of cold (warm) temperature anomalies underlying strong enhanced (suppressed) convection, is virtually absent over the Indian Ocean in NCEP reanalysis data. In contrast to the sharp and well-defined transition between warm (cold) and cold (warm) anomalies in the middle-lower troposphere in AIRS, the vertical temperature profiles in NCEP are less organized, possibly owing to the scarcity of conventional data to constrain the reanalysis.

[38] A diagram similar to Figure 8 but based on NCEP reanalysis is shown in Figure 10. In contrast to the results from AIRS, both the moisture and temperature preconditioning are virtually absent in NCEP data. Also in the strong suppressed (enhanced) convection region in phase one (phase five), there is a unanimous positive temperature anomaly below 400 hPa. This is quite different from that of the AIRS data, in which cold (warm) anomaly overlies warm (cold) anomaly in the strong suppressed (enhanced) convection region. Given the scarcity of radiosondes and other conventional data over the Indo-Pacific warm pool, the NCEP is mostly model-driven and the errors such as parameterization deficiency in the reanalysis may contribute to the difference between AIRS and NCEP [*Tian et al.*, 2006].

4. Summary and Discussion

[39] Data from several satellites (Aqua/AIRS 3-D air temperature/moisture; rainfall and SST from TRMM TMI; QuikSCAT surface wind) are synthesized to document the BSISO between 2003 and 2006, with the focus on the evolution of 3-D moist and temperature fields and underlying air-sea interactions. Eight phases of the BSISO are separated on the basis of the seasonally independent ISO index developed by *Wheeler and Hendon* [2004]. The composite CAPE, SST, surface convergence/divergence, 3-D water-vapor and air-temperature structures are analyzed. The horizontal structures of the composite BSISO reveal coherent spatial-temporal evolutions of intraseasonal CAPE, SST, surface wind, and rainfall anomalies in the Indo-Pacific warm pool region. The first half of the composite cycle is characterized by the eastward movement of BSISO convection, which reaches its maximum and starts to bifurcate at the west boundary of the Maritime Continent; whereas the second half of the composite cycle is characterized by a broad northwest-southeast tilting rainband, which links the north branch of the Indian Ocean convection and the equatorial western Pacific and moves northeastward and then dissipates.

[40] Atmosphere-ocean conditions jointly guide the convection of the BSISO. The composite results reveal that CAPE, SST, and surface wind convergence lead convection in both north and east directions. The SST could only partially contribute to the CAPE preconditioning given the phase lag between them. We conjecture that other factors such as radiative cooling (warming) may also contribute to it. Nevertheless, this needs to be proved through further numerical modeling in the future. On the other hand, ocean positively feeds back to the atmosphere from bottom up.

There is a smooth transition from boundary layer moistening, shallow convection at lower or middle troposphere, to the deep convection all through the troposphere. In the strongly enhanced (suppressed) convection region, moist (dry) anomalies usually occupy the whole troposphere, with dry (moist) anomalies lying in a very thin near-surface layer; whereas the transition from warm (cold) anomalies to cold (warm) anomalies is more distinct and occurs at a much higher altitude around 500–700 hPa. In the weakly enhanced (suppressed) convection region, moist (dry) anomalies overlie dry (moist) anomalies to the west/north of positive (negative) precipitation maximum.

[41] In the zonal direction, the preconditioning of the moist (dry) anomalies at the boundary layer to the subsequent positive (negative) rainfall maximum is about 60–90 degrees in longitude and quarter-to-half cycle in time. The preconditioning of warm (cold) anomalies is not well tilted compared to the preconditioning of moist (dry) anomalies. To the east of the large maximum precipitation anomaly center, the weak positive temperature anomalies could occupy the whole troposphere, which is possibly owing to the Kelvin wave response to the deep convection to the west.

[42] In the meridional direction, the preconditioning of the moist (dry) anomalies at the boundary layer to the subsequent positive (negative) rainfall maximum is as far as 15 degrees in latitude and a quarter-to-half cycle in time. As the convection strengthens and moves northward, the lead-lag relationships among CAPE, SST, surface convergence and rainfall are still well kept, although the actual spatial differences among them (degrees in latitude) are decreased. The southward tilting angle of moist anomalies is also decreased and the preconditioning of moist anomalies becomes less obvious. Note also that the amplitude of maximum positive precipitation anomalies varies as the BSISO propagates northward, reaches its climax around 10°N, implying the possible impact of annual cycle on the amplitude of intraseasonal variability.

[43] In the frictional "convective interaction with dynamics" (CID) theory of ISO [*Wang*, 1988, 2005; *Wang and Rui*, 1990b; *Wang and Li*, 1994], the boundary layer frictional moisture convergence-induced condensational heating plays an essential role in guiding the movement and development of low-frequency equatorial Kelvin-Rossby packages that characterize the ISO. The AIRS-observed low-level water-vapor and air-temperature preconditioning structures are consistent with this CID theory. For the eastward movement, the surface convergence slightly leads the materialization of deep convection, suggesting the pivotal role of frictional moist convergence in integrating the condensational heating, low-frequency equatorial Kelvin-Rossby waves, boundary layer dynamics, moisture feedback, and wind-induced heat exchanges at the surface [*Wang*, 2005; *Tian et al.*, 2006].

[44] However, there are many other factors that may contribute to the complexity of tropical intraseasonal phenomenon. The evaporation cooling and associated downdrafts underlying enhanced convection may contribute to the temperature and moisture preconditioning of the suppressed convection behind, although current satellite observation cannot give a definite answer because of retrieval uncertainties. In addition, the northward propagation of BSISO can be generated by easterly vertical shear [*Drbohlav and Wang*, 2005; *Jiang et al.*, 2004], advection of mean state specific humidity by meridional wind [*Jiang et al.*, 2004] and the intraseasonal variation of SST [*Kemball-Cook and Wang*, 2001; *Fu et al.*, 2003]. All these factors may play a complimentary role in the maintenance and growth of BSISO.

[45] **Acknowledgments.** The authors wish to thank Diane Henderson for editing the text. This work was supported by NASA Earth Science Program, NSF Climate Dynamics Program, and by the Japan Agency for Marine-Earth Science and Technology (JAMSTEC), NASA, and NOAA through their sponsorship of the IPRC. This paper is SOEST contribution 7332 and IPRC contribution 510.

References

Drbohlav, H.-K. L., and B. Wang (2005), Mechanism of the northward propagating intraseasonal oscillation in the south Asia monsoon region: Results from a zonally averaged model, *J. Clim.*, *18*, 952–972, doi:10.1175/JCLI3306.1.

Eskridge, R. E., O. A. Alduchov, I. V. Chernykh, P. Zhai, A. C. Polansky, and S. R. Doty (1995), A Comprehensive Aerological Reference Data Set (CARDS): Rough and systematic errors, *Bull. Am. Meteorol. Soc.*, *76*, 1759–1775, doi:10.1175/1520-0477(1995)076<1759:ACARDS>2.0.CO;2.

Flatau, M., P. Flatau, P. Phoebus, and P. Niller (1997), The feedback between equatorial convection and local radiative and evaporative processes: The implication for intraseasonal oscillations, *J. Atmos. Sci.*, *54*, 2373–2386, doi:10.1175/1520-0469(1997)054<2373:TFBECA>2.0.CO;2.

Fu, X., B. Wang, T. Li, and J. P. McCreary (2003), Coupling between northward-propagating, intraseasonal oscillations and surface temperature in the Indian Ocean, *J. Atmos. Sci.*, *60*, 1733–1753, doi:10.1175/1520-0469(2003)060<1733:CBNIOA>2.0.CO;2.

Fu, X., B. Wang, and L. Tao (2006), Satellite data reveal the 3-D moisture structure of tropical intraseasonal oscillation and its coupling with underlying ocean, *Geophys. Res. Lett.*, *33*, L03705, doi:10.1029/2005GL025074.

Fu, X., B. Wang, D. Waliser, and L. Tao (2007), Impact of air-sea coupling on the predictability of monsoon ISO, *J. Atmos. Sci.*, *64*, 157–174, doi:10.1175/JAS3830.1.

Gibson, J. K., P. Kallberg, S. Uppala, A. Hernandez, A. Nomura, and E. Serrano (1997), ERA description, *Re-analysis Proj. Rep. Ser. 1*, 72 pp., Eur. Cent. for Medium-Range Weather Forecasts, Reading, U. K.

Gualdi, S., A. Navarra, and H. von Storch (1997), Tropical intraseasonal oscillation appearing in operational analyses and in a family of general circulation models, *J. Atmos. Sci.*, *54*, 1185–1202, doi:10.1175/1520-0469(1997)054<1185:TIOAIO>2.0.CO;2.

Hendon, H. H., and B. Liebmann (1990), The intraseasonal (30–50 day) oscillation of the Australian summer monsoon, *J. Atmos. Sci.*, *47*, 2909–2923, doi:10.1175/1520-0469(1990)047<2909:TIDOOT>2.0.CO;2.

Hendon, H. H., and M. L. Salby (1994), The life cycle of the Madden-Julian oscillation, *J. Atmos. Sci.*, *51*, 2225–2237, doi:10.1175/1520-0469(1994)051<2225:TLCOTM>2.0.CO;2.

Houze, R. A., Jr., S. S. Chen, D. K. Kingsmill, Y. Serra, and S. E. Yuter (2000), Convection over the Pacific warm pool and in relation to the atmospheric Kelvin-Rossby wave, *J. Atmos. Sci.*, *57*, 3058–3089, doi:10.1175/1520-0469(2000)057<3058:COTPWP>2.0.CO;2.

Jiang, X., T. Li, and B. Wang (2004), Structures and mechanisms of the northward propagating boreal summer intraseasonal oscillation, *J. Clim.*, *17*, 1022–1039, doi:10.1175/1520-0442(2004)017<1022:SAMOTN>2.0.CO;2.

Jones, C., and B. C. Weare (1996), The role of low-level moisture convergence and ocean latent heat fluxed in the Madden and Julian oscillation: An observational analysis using ISCCP data and ECMWF analyses, *J. Clim.*, *9*, 3086–3104, doi:10.1175/1520-0442(1996)009<3086:TROLLM>2.0.CO;2.

Jones, C., D. E. Waliser, and C. Gautier (1998), The influence of the Madden-Julian oscillation on ocean surface heat fluxes and sea surface temperature, *J. Clim.*, *11*, 1057–1072, doi:10.1175/1520-0442(1998)011<1057:TIOTMJ>2.0.CO;2.

Kalnay, E., et al. (1996), The NCEP 40-year Reanalysis Project, *Bull. Am. Meteorol. Soc.*, *77*, 437–471, doi:10.1175/1520-0477(1996)077<0437:TNYRP>2.0.CO;2.

Kemball-Cook, S. R., and B. Wang (2001), Equatorial waves and air-sea interaction in the boreal summer intraseasonal oscillation, *J. Clim.*, *14*,

2923–2942, doi:10.1175/1520-0442(2001)014<2923:EWAASI>2.0.CO;2.
Kemball-Cook, S. R., and B. C. Weare (2001), The onset of convection in the Madden-Julian oscillation, *J. Clim.*, *14*, 780–793, doi:10.1175/1520-0442(2001)014<0780:TOOCIT>2.0.CO;2.
Kiladis, G. N., K. H. Straub, and P. T. Haertel (2005), Zonal and vertical structure of the Madden-Julian Oscillation, *J. Atmos. Sci.*, *62*, 2790–2809, doi:10.1175/JAS3520.1.
Krishnamurti, T. N., D. K. Oosterhof, and A. V. Mehta (1988), Air-sea interaction on the time scale of 30 to 50 days, *J. Atmos. Sci.*, *45*, 1304–1322, doi:10.1175/1520-0469(1988)045<1304:AIOTTS>2.0.CO;2.
Lau, K.-M., and C.-H. Sui (1997), Mechanisms of short-term sea surface temperature regulation: Observations during TOGA COARE, *J. Clim.*, *10*, 465–472, doi:10.1175/1520-0442(1997)010<0465:MOSTSS>2.0.-CO;2.
Lin, X., and R. H. Johnson (1996), Kinetic and thermodynamic characteristics of the flow over the western Pacific Warm Pool during TOGA/COARE, *J. Atmos. Sci.*, *53*, 695–715, doi:10.1175/1520-0469(1996)053<0695:KATCOT>2.0.CO;2.
Madden, R., and P. R. Julian (1971), Description of a 40–50 day oscillation in the zonal wind in the tropical Pacific, *J. Atmos. Sci.*, *28*, 702–708, doi:10.1175/1520-0469(1971)028<0702:DOADOI>2.0.CO;2.
Madden, R., and P. R. Julian (1972), Description of global scale circulation cells in the tropics with a 40–50 day period, *J. Atmos. Sci.*, *29*, 1109–1123, doi:10.1175/1520-0469(1972)029<1109:DOGSCC>2.0.CO;2.
Mapes, B. E., S. Tulich, J.-L. Lin, and P. Zuidema (2006), The mesoscale convection life cycle: Building block or prototype for large-scale tropical waves?, *Dyn. Atmos. Oceans*, *42*, 3–29, doi:10.1016/j.dynatmoce.2006.03.003.
McBride, J. L., and W. M. Frank (1999), Relationship between stability and monsoon convection, *J. Atmos. Sci.*, *56*, 24–36, doi:10.1175/1520-0469(1999)056<0024:RBSAMC>2.0.CO;2.
Meyers, D., and D. E. Waliser (2003), Three dimensional water vapor and cloud variation associated with the Madden-Julian Oscillation during northern hemisphere winter, *J. Clim.*, *16*, 929–950.
Rui, H., and B. Wang (1990), Development characteristics and dynamical structure of tropical intraseasonal convection anomalies, *J. Atmos. Sci.*, *47*, 357–379, doi:10.1175/1520-0469(1990)047<0357:DCADSO>2.0.CO;2.
Salby, M. L., R. R. Garcia, and H. H. Hendon (1994), Planetary-scale circulations in the presence of climatological and wave induced heating, *J. Atmos. Sci.*, *51*, 2344–2367, doi:10.1175/1520-0469(1994)051<2344:PSCITP>2.0.CO;2.
Sengupta, D., and M. Ravichandran (2001), Oscillations of Bay of Bengal sea surface temperature during the 1998 summer monsoon, *Geophys. Res. Lett.*, *28*, 2033–2036, doi:10.1029/2000GL012548.
Shinoda, T., H. H. Hendon, and J. Glick (1998), Intraseasonal variability of surface fluxes and sea surface temperature in the tropical western Pacific and Indian Oceans, *J. Clim.*, *11*, 1685–1702, doi:10.1175/1520-0442(1998)011<1685:IVOSFA>2.0.CO;2.
Spencer, R. W. (1993), Global oceanic precipitation from the MSU during 1979–91 and comparisons to other climatologies, *J. Clim.*, *6*, 1301–1326, doi:10.1175/1520-0442(1993)006<1301:GOPFTM>2.0.CO;2.
Sperber, K. R. (2003), Propagation and the vertical structure of the Madden-Julian oscillation, *Mon. Weather Rev.*, *131*, 3018–3037, doi:10.1175/1520-0493(2003)131<3018:PATVSO>2.0.CO;2.
Stephens, G. L., P. J. Webster, R. H. Johnson, R. Englen, and T. L'Ecuyer (2004), Observational evidence for the mutual regulation of the tropical hydrological cycle and tropical sea surface temperatures, *J. Clim.*, *17*, 2213–2224, doi:10.1175/1520-0442(2004)017<2213:OEFTMR>2.0.CO;2.
Susskind, J., P. Piraino, L. Rokke, L. Iredell, and A. Mehta (1997), Characteristics of the TOVS Pathfinder Path A Dataset, *Bull. Am. Meteorol. Soc.*, *78*, 1449–1472, doi:10.1175/1520-0477(1997)078<1449:COTTPP>2.0.CO;2.
Tian, B., D. E. Waliser, E. J. Fetzer, B. H. Lambrigtsen, Y. L. Yung, and B. Wang (2006), Vertical moist thermodynamic structure and spatial–temporal evolution of the MJO in AIRS observations, *J. Atmos. Sci.*, *63*, 2462–2485, doi:10.1175/JAS3782.1.
Waliser, D. E., K. M. Lau, and J. J. Kim (1999), The influence of coupled sea surface temperatures on the Madden-Julian oscillation: A model perturbation experiment, *J. Atmos. Sci.*, *56*, 333–358, doi:10.1175/1520-0469(1999)056<0333:TIOCSS>2.0.CO;2.
Waliser, D. E., W. Stern, S. Schubert, and K. M. Lau (2003), AGCM simulations of intraseasonal variability associated with the Asian summer Monsoon, *Clim. Dyn.*, *21*, 423–446, doi:10.1007/s00382-003-0337-1.
Wang, B. (1988), Dynamics of tropical low-frequency waves: An analysis of the moist Kelvin wave, *J. Atmos. Sci.*, *45*, 2051–2065, doi:10.1175/1520-0469(1988)045<2051:DOTLFW>2.0.CO;2.
Wang, B. (2005), Theories, in *Intraseasonal Variability in the Atmosphere-Ocean Climate System*, edited by K. M. Lau and D. E. Waliser, chap. 10, pp. 307–360, Springer, New York.
Wang, B., and T. Li (1994), Convective interaction with boundary-layer dynamics in the development of a tropical intraseasonal system, *J. Atmos. Sci.*, *51*, 1386–1400, doi:10.1175/1520-0469(1994)051<1386:CIWBLD>2.0.CO;2.
Wang, B., and H. Rui (1990a), Synoptic climatology of transient tropical intraseasonal convection anomalies: 1975–1985, *Meteorol. Atmos. Phys.*, *44*, 43–61, doi:10.1007/BF01026810.
Wang, B., and H. Rui (1990b), Dynamics of the coupled moist Kelvin-Rossby wave on an equatorial beta plane, *J. Atmos. Sci.*, *47*, 397–413, doi:10.1175/1520-0469(1990)047<0397:DOTCMK>2.0.CO;2.
Wang, B., and X. Xie (1998), Coupled modes of the warm pool climate system. part I: The role of air–sea interaction in maintaining Madden–Julian oscillation, *J. Clim.*, *11*, 2116–2135.
Wang, B., P. J. Webster, and H. Teng (2005), Antecedents and self-induction of active-break south Asian monsoon unraveled by satellites, *Geophys. Res. Lett.*, *32*, L04704, doi:10.1029/2004GL020996.
Wang, W., and M. E. Schlesinger (1999), The dependence on convection parameterization of the tropical intraseasonal oscillation simulated by the UIUC 11-layer atmospheric GCM, *J. Clim.*, *12*, 1423–1457, doi:10.1175/1520-0442(1999)012<1423:TDOCPO>2.0.CO;2.
Webster, P. J., and R. Lukas (1992), TOGA COARE: The Coupled Ocean—Atmosphere Response Experiment, *Bull. Am. Meteorol. Soc.*, *73*, 1377–1416, doi:10.1175/1520-0477(1992)073<1377:TCTCOR>2.0.CO;2.
Weickmann, K. M. (1983), Intraseasonal circulation and outgoing longwave radiation modes during Northern Hemisphere winter, *Mon. Weather Rev.*, *111*, 1838–1858, doi:10.1175/1520-0493(1983)111<1838:ICAOLR>2.0.CO;2.
Wheeler, M., and H. Hendon (2004), An all-season real-time multivariate MJO index: Development of an index for monitoring and prediction, *Mon. Weather Rev.*, *132*, 1917–1932, doi:10.1175/1520-0493(2004)132<1917:AARMMI>2.0.CO;2.
Yanai, M., B. Chen, and W. Tung (2000), The Madden-Julian oscillation observed during the TOGA COARE IOP: Global view, *J. Atmos. Sci.*, *57*, 2374–2396, doi:10.1175/1520-0469(2000)057<2374:TMJOOD>2.0.CO;2.
Zhang, C. D., and H. H. Hendon (1997), Propagating and standing components of the intraseasonal oscillation in tropical convection, *J. Atmos. Sci.*, *54*, 741–752, doi:10.1175/1520-0469(1997)054<0741:PASCOT>2.0.CO;2.

X. Fu, B. Wang, and B. Yang, International Pacific Research Center, University of Hawaii at Manoa, 1680 East West Road, POST Building, 4th Floor, Honolulu, HI 96822, USA. (yangbo@hawaii.edu)